

Dynamical Properties of Molecular Cloud Complexes in a Redshift 6 Prototypical Galaxy at the Epoch of Reionization

T. K. Daisy Leung^{1, 2}, Andrea Pallottini^{3, 4}, Andrea Ferrara^{4, 5}, and Mordecai-Mark Mac Low^{2, 6, 7, 8}

¹ Department of Astronomy, Space Sciences Building, Cornell University, Ithaca, NY 14853, USA; tleung@astro.cornell.edu

² Center for Computational Astrophysics, Flatiron Institute, 162 Fifth Avenue, New York, NY 10010, USA

³ Centro Fermi, Museo Storico della Fisica e Centro Studi e Ricerche “Enrico Fermi”, Piazza del Viminale 1, Roma, 00184, Italy

⁴ Scuola Normale Superiore, Piazza dei Cavalieri 7, I-56126 Pisa, Italy

⁵ Kavli Institute for the Physics and Mathematics of the Universe (IPMU), The University of Tokyo, 5-1-5 Kashiwanoha, Kashiwa 277-8583, Japan

⁶ Institut für Theoretische Astrophysik, Zentrum für Astronomie der Universität Heidelberg, 69120 Heidelberg, Germany

⁷ American Museum of Natural History, 79th St. at Central Park West, New York, NY 10024, USA

⁸ Department of Physics, Disque Hall, Drexel University, Philadelphia, PA 19104, USA

Paper draft for the project developed at the Kavli Summer Program in Astrophysics 2018. To be Submitted.

Abstract

We study the dynamical properties of molecular clouds complexes (MC) and their temporal evolution in Althæa, a prototypical galaxy at the Epoch of Reionization (EoR) using state-of-the-art cosmological zoom-in simulation. We use a clump finder algorithm and a set of H₂ volumetric densities (n_{cut}) to identify MCs and their sub-structures. We extract properties such as mass, size, Mach number, velocity dispersion, gas surface density, and virial parameter for each MC and compare them with those observed in the Milky Way disk, the Galactic center, and gas-rich starburst galaxies in the local Universe and at the peak epoch of cosmic star formation. The high velocity dispersions found in the MCs of Althæa ($\gtrsim 100 \text{ km s}^{-1}$) are comparable to those observed in starburst galaxies. The mass scale of the MCs is of the order of $10^{6.5-9} M_{\odot}$. The $\sim 200 \text{ pc}$ -scale MCs found with a low density threshold correspond to the spiral arms of Althæa which break down into smaller $\lesssim 100 \text{ pc}$ -scale MCs at higher density thresholds. The more massive and bigger MCs in Althæa compared to the Milky Way likely result from the higher gas mass fraction, surface density, and velocity dispersion, which set the scale for fragmentation. The MCs of Althæa are found to have higher σ and Σ systematically regardless of the n_{cut} adopted. The velocity dispersion remains $\gtrsim 100 \text{ km s}^{-1}$ even when we increase the n_{cut} and even for the molecular substructures, likely resulting from the strong supernova and stellar feedback Althæa experienced over the multiple episodes of bursty star formation. Virial analysis indicates that the MC found in the arms of the main disk of Althæa are unbound, but the substructures have lower virial parameter. This is consistent with the notion that collapsing structures result from gravitational instability within globally stable structures, which are supported by turbulence and rotation on large scale. We also find $\alpha_{\text{vir}} \sim 1$ for the MCs in the satellite galaxies, which we interpret as a result of the weaker stellar feedback as they have experienced less episodes of star formation compared to Althæa (also supported by the lower stellar-to-gas mass ratio of the latter). MCs in the satellites are therefore likely collapsing structures. This paints a picture, in which at the EoR, star formation continues as gas is being accreted from the IGM. We find no temporal variations in the MC dynamics over the course of 700 Myr traced in our simulation, at least in terms of the scaling relations examined. Our results are independent of the volume density threshold adopted, except for the slope of the cumulative mass distribution, which steepens as we increase n_{cut} . High resolution imaging of the first galaxies with the Atacama Large (sub-)Millimeter Array (ALMA) and the Next Generation Very Large Array (ngVLA) will provide useful observational data to test our findings and the validity of our simulation to shed light on star formation since the cosmic dark ages.

Keywords: methods: data analysis – galaxies: high-redshift – galaxies: ISM – galaxies: evolution – galaxies: formation – galaxies: starburst – stars: formation

1. Introduction

The growth of galaxies and their subsequent evolution are governed by the baryon cycle — galaxies accrete gas from the intergalactic medium (IGM) to fuel star formation (and feed their supermassive blackholes) and subsequent feedback replenishes and enriches the circumgalactic medium with part of this material. The general consensus is that the growth of high- z galaxies are triggered and supported by massive gas inflows from mergers and/or the cosmic web at early cos-

mic time, when the IGM and galaxies themselves are more gas-rich in their star-forming molecular gas contents compared to present-day galaxies. These massive gas inflows in turn trigger gravitational instability and lead to the formation of gas structures that are typically more massive and denser than those observed in nearby galaxies, with masses of $M_{\text{cl}} = 10^9 M_{\odot}$ and sizes on sub-kpc scales (e.g., Gabor & Bournaud 2013; Hopkins et al. 2014; Inoue et al. 2016). Some theoretical works argue that the migration of such mas-

sive clumps are responsible for contributing to the buildup of the bulges of massive galaxies at $z \sim 0$ (e.g., Ceverino et al. 2010).

Given that high- z galaxies are the early stages of evolution of present-day galaxies, studying their ISM properties is essential for understanding how star formation proceed under these more extreme conditions, thereby driving the evolution and assembly history of galaxies since the cosmic dark ages. Current consensus is that at higher redshifts, galaxies have higher star formation rates (SFR; Behroozi et al. 2013; Sparre et al. 2015; Maiolino et al. 2015; Dunlop et al. 2017) and smaller sizes (e.g., Bouwens et al. 2011; Ono et al. 2013) compared to those found in the local Universe. The former are thus expected to have more H II regions, ionized gas, and more intense radiation stellar feedbacks. Since their metallicity and dust content are also expected to be lower as they are assembling, this affects the shielding of UV photons, heating and cooling mechanisms in these early systems. Such differences in turn affect the regulation of thermal and chemical structures of their ISM. Their multi-phase ISM and the dynamics of the star-forming molecular cloud complexes (MC) are therefore expected to differ from nearby galaxies. Even in the local Universe, where the most detailed observations can be attained, variations in cloud properties have been observed between different galaxy populations (see e.g., Hughes et al. 2010, 2013). It is thus intuitive and reasonable to pose the question: what are the dynamical states of the MCs of the first galaxies and how do they differ from the local Universe, and are they analogous to any seen in the local galaxy populations?

The FIR fine-structure lines (e.g., [CII], [NII], and [OIII]), and CO/[CI] lines are the key diagnostics for constraining the ISM conditions of galaxies and provide highly complementary information tracing the different phases of the ISM (ionized, atomic, molecular; e.g., Scoville & Solomon 1974; Rubin 1985; Malhotra et al. 2001). Global measurements of these diagnostics in high- z galaxies have informed us on their galaxy-wide properties (e.g., gas masses, gas temperature, and radiation field intensity). However, spatially resolving their ISM is needed in order to understand their role in galaxy evolution and the physics behind their intense star formation ($\text{SFR} \sim 100 - 3000 M_{\odot} \text{ yr}^{-1}$). To date, spatially resolved ISM properties of high- z galaxies have only been examined observationally in a handful of (strongly-lensed) galaxies, using tracers such as dust continuum, CO, and [CII] lines (e.g., Swinbank et al. 2011; Hodge et al. 2015; Ferkinhoff et al. 2015; Hodge et al. 2016, Leung et al. 2018, submitted). These studies find that galaxies at $z \sim 2$ galaxies, close to the peak of cosmic star formation, are more molecular gas-rich, turbulent, and clumpy than nearby galaxies. That said, it remains unclear how star formation proceed in the (sub-) L^* galaxy population at $z \gtrsim 6$ — the epoch of reionization — which is responsible for producing the ionizing photons that reionized the Universe.

While ALMA has enabled the detections of ISM diagnostic lines e.g., the [CII] $158 \mu\text{m}$ and CO line emission in normal ($\text{SFR} < 100 M_{\odot} \text{ yr}^{-1}$) galaxies at $z > 6$ over the past few years (e.g., Smit et al. 2018), we are still far from mapping their molecular ISM due to the cosmological dimming. As such, we have undertaken a study, exploiting state-of-the-art cosmological zoom-in hydrodynamic simulation SERRA (Greenhouse in Italian; Pallottini et al. 2017b,a), to examine the dynamical properties of the molecular cloud complexes in a $z \sim 6$ prototypical (i.e., L^*) galaxy.

This paper is structured as follows. ~~(AP: TBM)~~ In §2, we describe the setup of our simulation and the properties of our galaxy (Althæa), and describe the method used to identify its molecular gas complexes (MC). In §3, we present scaling relations based on the MC identified and compare them with observations of molecular (sub-)structures seen in nearby and $z > 0$ galaxies. We present Toomre stability analysis in §4 and the cumulative mass distribution of the MCs in Althæa in §5. In §6, we discuss the results and implications of our findings, and present our conclusions in §7. Throughout this paper, we adopt a concordance cosmology, with total matter density $\Omega_{\Lambda} = 0.692$, $\Omega_m = 0.308$, $\Omega_b = 0.0481$, Hubble constant $H_0 = 100 h \text{ km s}^{-1} \text{ Mpc}^{-1}$ with $h = 0.678$, spectral index $n = 0.967$ and $\sigma_8 = 0.826$ (Planck Collaboration et al. 2014).

2. Method: Simulation and “Clump”-finding

2.1. SERRA Simulation⁸

The simulation used in this work is described by Pallottini et al. (2017b) and is briefly summarized here.

SERRA is a cosmological zoom-in simulation performed using Eulerian hydrodynamics and adaptive mesh refinement (AMR) technique to achieve high spatial resolution in the region of interest (i.e., regions of high baryonic density). In particular, it uses a modified version of RAMSES (Teyssier 2002) as the AMR backend. Our simulation covers a comoving box of $20 \text{ Mpc } h^{-1}$ in size, resolving down to a physical scale of $l \approx 30 \text{ pc}$ (at $z \sim 6$) and a (baryonic) mass resolution of $m_b \simeq 10^4 M_{\odot}$ in the finest level. Such a physical scale is close to the size scale of molecular cloud complexes and giant molecular clouds (GMCs), as seen in nearby galaxies (e.g., Sanders et al. 1985; Federrath & Klessen 2013; Goodman et al. 2014). We include chemical network in the simulation to trace H, H^+ , H^- , He, He^+ , He^{++} , H_2 , H_2^+ (Grassi et al. 2014; Bovino et al. 2016). Of particular importance to our study here is that our simulation includes non-equilibrium formation of molecular hydrogen (done on-the-fly) to determine the H_2 abundance (see Pallottini et al. 2017a for effects of chemistry affected by non-equilibrium versus equilibrium H_2 formation).

Star formation is modeled using a H_2 -based prescription of

⁸ Serra means greenhouse in Italian which is motivated by the fact that our simulation includes a chemical network to calculate the abundance of H_2 , which in turn dictates the formation of CO.

the Schmidt-Kennicutt relation (Krumholz et al. 2009). We adopt stellar tracks from STARBURST99 and include stellar feedback from supernovae and OB/AGB stars to account for energy dissipations. To couple the feedback to the gas, we employ sub-grid modeling for blastwaves, e.g., to account for the potential lost of energy inside the cell when supernovae explode. The energy dissipated is then injected into the ISM in the form of kinetic and thermal energy. Radiation pressure on the dust and gas is also included (see Pallottini et al. 2017b for details).

Details on the properties of Althæa — the main galaxy in our simulation — are discussed in Pallottini et al. (2017a). Briefly, by $z \sim 6$, Althæa is a Lyman-break galaxy (LBG) hosted in a dark matter halo of mass $M_{\text{DM}} \simeq 10^{10} M_{\odot}$ at the center of a cosmic web knot, and accretes mass from the IGM mainly via three filaments of length $\simeq 100$ kpc. At $z \sim 6$, Althæa has a stellar mass of $M_* \simeq 3 \times 10^{10} M_{\odot}$, a metallicity of $Z \simeq 0.5 Z_{\odot}$, a molecular gas mass of $M_{\text{H}_2} \simeq 5 \times 10^7 M_{\odot}$, and a globally-integrated SFR of $\simeq 100 M_{\odot} \text{ yr}^{-1}$. It is therefore a prototypical galaxy at $z \sim 6$.

The simulation data contain information such as the density (ρ) and velocity (v_x , v_y , and v_z) fields, from which we calculate the physical properties of each MC, such as mass and velocity dispersion. Due to the nature of our AMR simulation, we regrid the simulation data into uniform grids for the analysis presented in this paper. The grid size is defined based on the highest resolution of the simulation data (i.e., the less refined regions are supersampled in the resulting uniform grids).

2.2. Star Formation History

One of the advantage of studying the dynamical properties of molecular structures at $z \sim 6$ in simulation is the fact that we can examine how their properties evolve as a function of time. This is advantageous especially at early cosmic epochs, when densest structures are beginning to form; gas is constantly being accreted onto the central galaxy from the cosmic web and satellite galaxies, thereby leading to bursts of star formation. Meanwhile, tidal forces resulting from interactions with these surrounding galaxies can disrupt the main disk and arms, likely leading to different dynamical states for the molecular structures compared to more evolved galaxies found at a later cosmic time (e.g., some molecular structures may disperse while others may agglomerate into more massive ones).

We show the star formation history of Althæa in Figure 1, where the SFR of Althæa varies between $\sim 30 - 80 M_{\odot} \text{ yr}^{-1}$ as it evolves from an actively accreting phase to a starburst phase after a major merger, and then back to a relatively quiescent phase over the few hundred Myr simulated in our simulation. The SFR of Althæa is calculated based on existing

⁹ The SFR plotted in Figure 2 of Pallottini et al. (2017a) is a factor of two higher than shown here since they also include contributions from massive satellites galaxies within the surrounding ≈ 50 kpc, which are accreted onto Althæa at $z \lesssim 2$.

young stellar population, which is defined to have an age of $t_{\text{age}} < 10$ Myr.

Given the stochasticity in the star formation history of Althæa, we show the scaling relations found for two particular snapshots/evolutionary stages of Althæa as examples in §3.2 to illustrate the salient points of the discussion, since they represent the extreme evolutionary stages of Althæa (and thus, likely bracket the most extreme variations in the cloud dynamics) — one of which Althæa is actively accreting materials from its surrounding and another of which Althæa is undergoing a starburst phase after a major merger (see Figure 1).

2.3. Structure identification

To identify the molecular complexes, we use a customized version of the clump finder algorithm available in the PYTHON package YT (Turk et al. 2011), which was initially described in Smith et al. (2009), but this function has been modified since then. The latest version of the default YT clump finder decomposes the zones in the simulation into non-overlapping tiles, which are stored in a k-dimensional tree (aka k-d tree). It then identifies the contours of a variable field (here, the density field) within a tile and connects them across the tiles. In the customized version used for this study, we modify the function to enhance the stability of the code (which essentially means ~~fixed the bugs in order for it to actually work~~).

In the “clump-finding” process, we employ a set of different density thresholds defined based on the molecular hydrogen density of Althæa taken at different cosmic times (between $z = 6.0 - 7.2$). We note that this process is in essence similar to identifying molecular structures based on the noise levels of surface density maps observers obtain with telescopes, using molecular line tracers such as CO, CS, and HCN, as commonly adopted in observational studies (e.g., identifying “clumps” based on/after applying σ -clipping, using tools such as AIPS’s task SERCH, CLUMPFIND, and CPROPS; Williams et al. 1994; Oka et al. 2001; Rosolowsky & Leroy 2006). We note that, owing to the nature of observations, such structures are identified in position-position-velocity (PPV) space, whereas in simulations, one has the full 6D spatial-kinematic information, and can therefore cleanly identify structures directly using the density field in position-position-position (PPP) space. Existing studies find a good correspondence in the dynamical properties extracted in PPV- versus PPP-space (Ballesteros-Paredes & Mac Low 2002; Heitsch et al. 2009; Shetty et al. 2010; Beaumont et al. 2013; Pan et al. 2015; Ibáñez-Mejía et al. 2016, but see also Shetty et al. 2010 for a discussion on caveats and limitations).

In Figure 2, we show an example of the volumetric H_2 density (n_{H_2}) distribution of Althæa given snapshot which includes contributions from its surrounding 7 kpc (in diameter)¹⁰. We note that the distribution is almost flat for

¹⁰ For reference, the half mass radius of Althæa is ~ 0.5 kpc and the dark matter virial radius at which the mean enclosed density is 200 times the critical density of the Universe is $r_{200} \sim 15$ kpc.

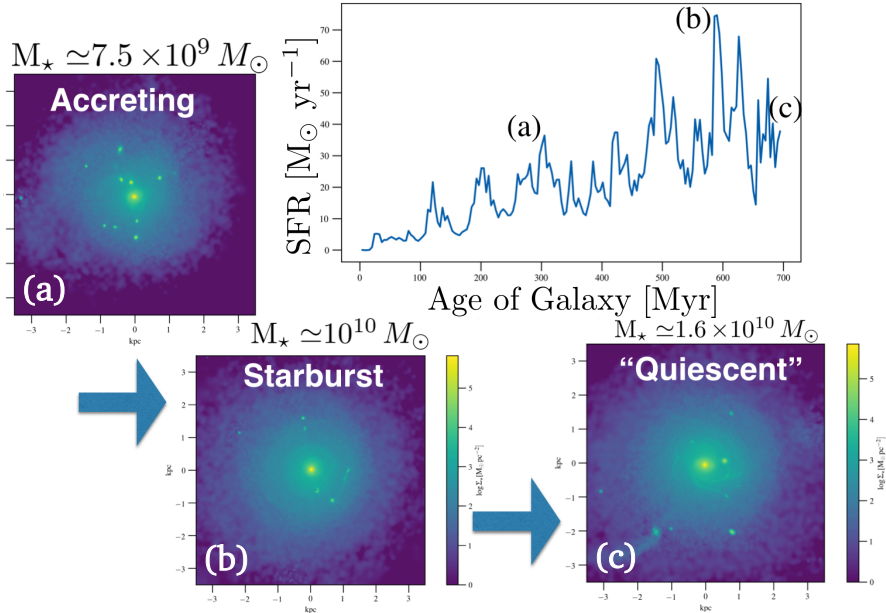


Figure 1. Star formation history of Althaea (top right) and projected stellar mass distribution of Althaea during one of its accretion phases at its early stage of evolution (a); during one of its major starburst phases after a major merger (b); and in a relatively quiescent phase post-starburst (c).

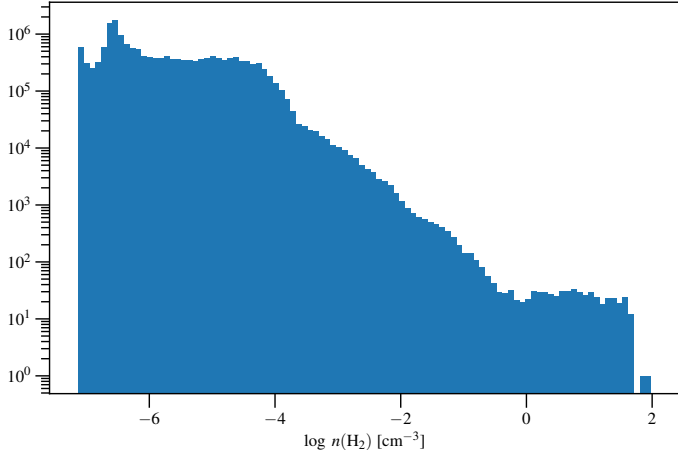


Figure 2. Volumetric H₂ density distribution of Althaea taken from a single snapshot, corresponding to the accreting phase shown in Figure 1.

$n_{\text{H}_2} \gtrsim 1 \text{ cm}^{-3}$ and it samples the range of density where “clumps/structures” are found based on the Euler characteristic, i.e., the fourth Minkowsky functional (see Appendix of Pallottini et al. 2017a). In Figure 3, we show an example of the molecular structures identified by applying volumetric H₂ density cuts of $n_{\text{cut}} = [0.32, 0.53, 0.88, 1.45, 2.45, 4.08, 6.81, 11.36, 19.00, 31] \text{ cm}^{-3}$ ¹¹ to the same snapshot as that used to plot Figure 2. Since the molecular structures identified could easily appear as overlapping structures depending on the viewing angle, we also plot them in different three-dimensional projections — so that one can more easily see that they are collections of disjoint structures. We repeat

¹¹ Based on 10^n , where n represents the 10 elements that are uniformly spaced between $[-0.5, 1.5]$ in linear space. We also vary the range of n_{cut} adopted and find no qualitative differences affecting the results and conclusions of this work except in the slope of the CMF (see §3.3 and §5).

this identification process for 14 snapshots between redshift $z \in [6.0, 7.2]$, spaced by $\Delta t = 50 \text{ Myr}$.

Limited by the spatial resolution of our simulation ($l_{\text{cell}} \approx 30 \text{ pc}$), we impose an additional constraint such that an identified structure only survives if it spans at least 10 cells in PPP space. We caution that one caveat of such constraint is that we can only examine the parameter space of “cloud” scaling relations at “cloud” size $R \gtrsim 100 \text{ pc}$.

3. Results: Cloud Scaling Relations

(AP: I see 2 main possible approaches to the presentation of the results (a) focus on a single snapshot, analyze the cloud scaling relation by varying the cuts and then by varying the snapshot; after that one can discuss the stability/toomre analysis of the clumps (help in discussing the origin) and the CMF. (b) discuss each scaling relation one at a time; probably an introductory subsection is needed to explain that different cuts yields no qualitative differences. Note that – in both cases – alternatively toomre analysis can be done at the beginning of the result section(s). I think that (b) might be a little bit more appealing, since all the plots with similar quantities (e.g. the larson relation for multiple cuts and snapshots) are in the same place (or, even better, page).) (DL: agreed, but will move things around later, after the report and after most of the content is ready.)

Molecular clouds are the natal place for star formation, and thus, their structure and dynamics hold important clues to understanding the mechanisms and physics of formation and evolution of molecular structures and star formation. Upon identifying the molecular structures, we extract properties such as mass (M_{cl}), size (R), Mach number (\mathcal{M}), velocity dis-

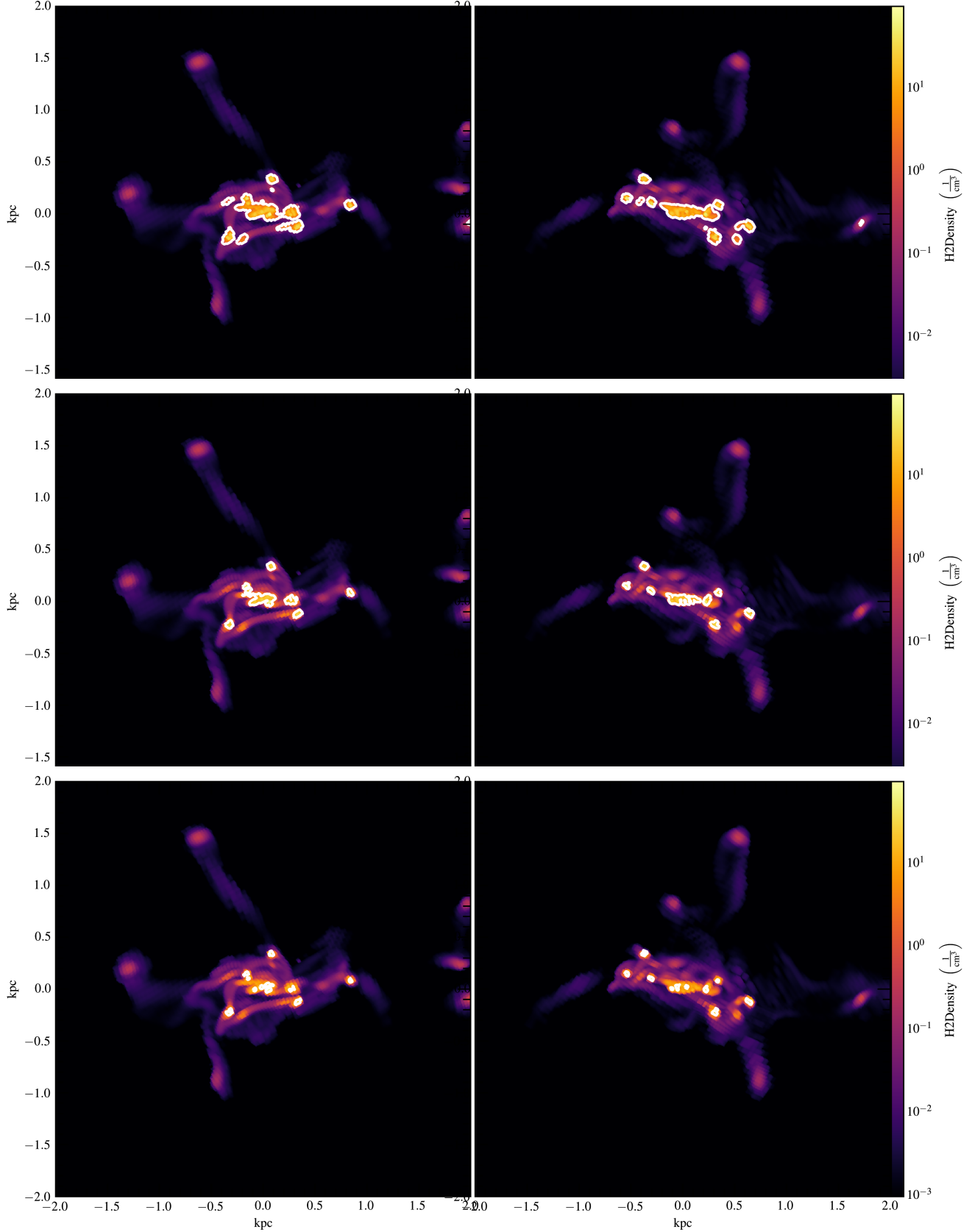


Figure 3. MC identified by applying volumetric H₂ density cuts of $n_{\text{cut}} = [0.32, 0.53, 0.88, 1.45, 2.45, 4.08, 6.81, 11.36, 19.00, 31.62] \text{ cm}^{-3}$. Color shows the projected H₂ surface density. **this should be H2 density 1/cm⁻²!?** (AP: if i recall correctly, this is not the projected h2 density, but the mass averaged h2 density field; additionally, we should convince yt to plot a proper label for the colorbar, and remove the trailing right axes labels (that are still there despite our efforts)) (DL: I tried more on Sept 7th, errrr, now all the ticks and labels for both panels disappear... hmm.. Not worth my time to fix this for the report.)



persion (σ), and gas surface density (Σ_{gas}) to examine their dynamics.

The mass of an MC is calculated from the uniformly-gridded 3D density field, integrating over all zones of the MC, multiplied by its volume. The size of an MC (R) is defined assuming spherical geometry (i.e., the size is parameterized via the radius of a sphere, which has a volume corresponding to that of the identified MC). Since in observations, dense gas contributes more to the observed linewidths than the more diffuse gas. We therefore calculate the one-dimensional non-thermal component of the velocity dispersion (σ_{NT}) of each MC as a density-weighted quantity:

$$\sigma_{\text{NT}}^2 = \frac{1}{3} \frac{\sum_{xyz} \sum_i^N \rho_i (\mathbf{v} - \bar{\mathbf{v}})_{xyz}^2}{\sum_i^N \rho_i}, \quad (1)$$

where N is the number of zones of each MC. The total velocity dispersion includes contributions from the thermal sound speed (c_s):

$$\sigma^2 = \sigma_{\text{NT}}^2 + c_s^2. \quad (2)$$

The local sound speed (c_s) of all identified molecular complexes are generally much smaller compared to the their turbulent velocities¹².

We show in Figure 4 the MC distributions in terms of their molecular gas masses, radii, and gas mass fractions, which we define as

$$f_{\text{gas}} = \frac{M_{\text{H}_2}}{(M_{\text{H}_2} + M_*)}, \quad (3)$$

where M_* is the stellar mass. We note that the distributions vary for different snapshots, depending on the evolutionary stage of Althæa. The highest surface density threshold of n_{cut} yields a “minimum” MC mass on the order of $10^{6.5} M_{\odot}$ for the densest MC identified. We find ~ 10 –13 MCs with masses exceeding $10^8 M_{\odot}$ across the snapshots for each of the given n_{cut} (see §2.3).

In the following subsections, we examine the MC properties in the context of the Larson’s relations (Larson 1981), which describe interactions between gravity and turbulence and is the first set of relations used for studying star-forming molecular structure formation based on observables (linewidth-size, density-size, and mass-size relations) and for comparing properties of molecular structures in different galactic environments. Observations of nearby gas-rich galaxies such as M64 and NGC 253 show higher velocity dispersions compared to the disk/mid-plane of the Milky Way which are, on the other hand, more consistent with those observed in the inner regions of Milky Way (Oka et al. 2001; Rosolowsky & Blitz 2005; Heyer et al. 2009; Leroy et al. 2015). While the velocity dispersions of the clouds in these nearby gas-rich

¹² We find comparable velocity dispersion between that derived from taking the root mean square versus that derived from thermal and non-thermal pressure terms, indicating that rotation velocity is unlikely to be the dominant source of velocity dispersion reported here. We further quantify the contributions arising from galactic rotation and shear to the extracted velocity dispersions of the MCs in §4. In the subsequent sections, we adopt the root mean square of the velocity field as the velocity dispersion (σ).

galaxies are comparable to the inner regions of Milky Way, they are found to be bigger in size (approximately an order of magnitude) and mass (approximately two orders of magnitude). These bigger clouds have been interpreted as a results of their higher gas mass fractions and surface densities and velocity dispersions, since fragmentation occurs near the Jeans length $L_J \propto \sigma^2/\Sigma$ and Jeans mass $M_J \propto \sigma^4/\Sigma$ for dispersion-supported structures.

3.1. Formalism: Virial Equilibrium and Larson’s Relations

A spherically symmetric cloud of mass M and radius R embedded within a medium of pressure P is described using the virial theorem:

$$\frac{1}{2} \ddot{I} = 2(T - T_s) + W + B, \quad (4)$$

where \ddot{I} is the second time derivative of the Lagrangian moment of inertia, T is the volume term of the total kinetic energy (including thermal and bulk motions), T_s is the surface term due to external thermal pressure, W is the gravity term, and B is the magnetic term. In the case where magnetic field is excluded (i.e., $B=0$), we can express this in terms of:

$$\frac{1}{2} \ddot{I} = 3M\sigma^2 - \frac{\Gamma GM^2}{R} - 4\pi P_{\text{ext}} R, \quad (5)$$

where the first term on the right hand side (RHS) is the pressure term from velocity dispersion, the second term is the gravity term, and the third term is the external pressure term. For the case of simple virial equilibrium (SVE; i.e., equilibrium state without external pressure), the LHS and the last term on the RHS vanish. The equation becomes:

$$\alpha_{\text{vir}} = \frac{3\sigma^2}{\Gamma GM/R} = \frac{5\sigma^2 R}{GM}, \quad (6)$$

where Γ is set to 3/5 for a uniform sphere. We can define

$$V_0^2 \equiv \frac{\sigma^2}{R}, \quad (7)$$

which is related to one of the Larson’s relations (linewidth-size relation), which can be recast into the form of:

$$\sigma^2/R = \pi G \Sigma / 5. \quad (8)$$

For pressure-bounded virial equilibrium (PVE; i.e. equilibrium state with pressure), Equation 5 becomes

$$P_{\text{ext}} = \frac{3\sigma^2 M}{4\pi R^3} - \frac{\Gamma GM^2}{4\pi R^4}, \quad (9)$$

which describes the external pressure needed to confine the gas inside a volume V . Rearranging the equation and substituting $\Sigma = M/\pi R^2$, we can express this equation using the following:

$$\frac{\sigma^2}{R} = \frac{1}{3} \left(\frac{4P_{\text{ext}}}{\Sigma} + \Gamma G \Sigma \pi \right). \quad (10)$$

Therefore, for a virialized cloud, one expects a one-to-one mapping between V_0^2 and Σ since $\sigma^2/R \propto \Sigma$, whereas Equation 10 represents the loci along which external pressures P_{ext}

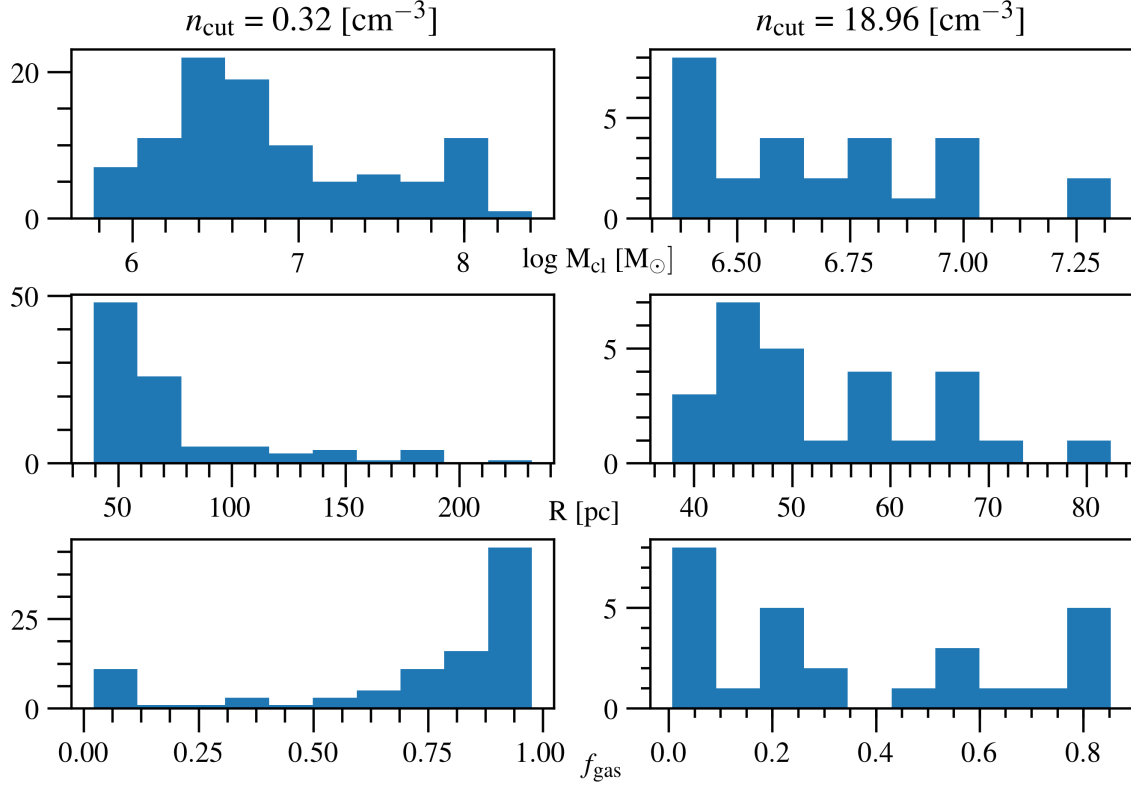


Figure 4. Distributions of masses, sizes, and gas mass fractions of MCs identified using the lowest n_{cut} (left panels) and $n_{\text{cut}} = 18.96 \text{ cm}^{-3}$ (right panels). Note the scale shown on the y-axes are different between the left and right panels, as less MCs are identified at higher n_{cut} .

are needed in order for MCs to have linewidths σ for a given set of surface densities (see bottom panels of Figure 6 and Figure 7). In other words, a cloud with σ and Σ offset from $\sigma^2/R \rightarrow \Sigma$ is in equilibrium with the external pressure P_{ext} (and therefore V_0^2 is not constant with Σ but varies depending on P_{ext} ; cf. expectation for SVE, where $\sigma \propto R^{0.5}$; see e.g., Heyer et al. 2009; Hughes et al. 2010, 2013; Meidt et al. 2013).

We use the virial parameter, which is defined using Equation 6 and describes the balance between kinetic and gravitational potential energies, to quantify how stable an MC is. An $\alpha_{\text{vir}} \approx 2$ corresponds to approximately equipartition between the two energy terms and is often used to assess the boundedness of a given structure (see e.g., Kauffmann et al. 2017)¹³.

3.2. Single Snapshots

(AP: I would move the following when discussing the velocity dispersion [yellow box]. Additionally, the large velocity dispersions was also noted in Vallini2018a, we can use some of those results to complement the discussion (e.g. shift for the CO sled at higher J than local galaxies).)

In each snapshot (see Figure 3 for example), we identify a set of MCs with consistently high turbulences and surface densities regardless of the H₂ density cuts adopted. These are the MCs at the center of the main disk of Althæa and occupy

the top right corner of the Larson's relation shown in Figure 5. (AP: however a plot showing the clump stats has not been show yet at this point) Their velocity dispersions are comparable to those observed in the inner Milky way and nearby gas-rich galaxies (e.g., M64; Oka et al. 2001; Rosolowsky & Blitz 2005; Heyer et al. 2009), along the locus of $\sigma \propto R^{0.56}$. Such high velocity dispersions and surface densities are expected since they are located in the nuclear regions of the galaxy, where the potential well is also deeper. The higher velocity dispersions in these MCs can also be understood as they have experienced more recent episodes of star formation as Althæa is assembling its stellar mass (these MCs also have higher stellar-to-gas mass ratios of ~ 60). In fact, by $z \simeq 7.2$ (i.e., the snapshot corresponding to the top panels of Figure 1 and Figure 5), Althæa has assembled a stellar mass of $M_* = 7.5 \times 10^9 M_\odot$. Thus, the higher velocity dispersion is due in part to the stronger stellar feedback compared to e.g., MCs in its satellite galaxies ($\sigma \approx 10 \text{ km s}^{-1}$).

As we increase the density threshold, some of the MC with [yellow box] the main disk break into multiple sub-MCs. As such, we effectively identify a population of denser molecular structures (Figure 3). This population of sub-MCs has dynamics largely similar to those observed in $z \sim 2$ spatially resolved studies of gas-rich star-forming galaxies, in terms of their velocity dispersions, sizes, and gas surface densities (Figure 5; see e.g., Swinbank et al. 2011), with sizes of the order of $R \simeq 100 \text{ pc}$ and velocity dispersions of $\sigma \simeq 20-80 \text{ km s}^{-1}$.

¹³ Note, however, that the true virial state/boundedness of a given structure also depends on the surface terms and the magnetic field (see Equation 5).

As shown in the top panel of Figure 6, their virial parameter ($\alpha_{\text{vir}} \gtrsim 10$) are lower than their “parent” MCs found in the main disk of Althæa ($\alpha_{\text{vir}} \gtrsim 100$).

We also compare the MCs identified in our simulations to those observed in the Milky Way in the context of the $\sigma^2/R - \Sigma$ relation (see bottom panel of Figure 6). The V-shaped dashed lines in the figure show the locii along which the given external pressures are needed for MCs to have linewidth for a given set of surface densities (see §3.1).

The lower α_{vir} and P_{ext} compared to their parent MCs are consistent with the conventional wisdom that collapsing structures result from local gravitational instability within globally non-collapsing structures (see e.g., Ballesteros-Paredes et al. 2011), which are supported by turbulence and rotation. In fact, based on the virial parameter, velocity dispersion, and pressure of the MC identified in the main disk of Althæa, the MC itself is gravitationally unbound and is supported/confined by turbulence (from the feedback of multiple episodes of star formation) and galactic rotation on large scales (occupying the high pressure region shown in the bottom panel of Figure 6).

The MCs in the satellite galaxies are found to have lower virial parameters compared to the (sub-)MCs in the main disk of Althæa, with $\alpha_{\text{vir}} \approx 2$. Differences in their α_{vir} most likely result from the weaker stellar feedback in the satellite galaxies as they have experienced less episodes of star formation compared to Althæa (i.e., lower stellar-to-gas mass ratios of ~ 0.1). In addition, the MCs in the satellite galaxies follow the locus of $\log(P/\text{K cm}^{-3}) = 6$ (see bottom panel of Figure 6). Given the low virial parameter and the $\sigma^2/R - \Sigma$ relation found for these MCs in the satellite galaxies, these structures are likely collapsing structures. This paints a picture, in which star formation continues as gas from the satellite galaxies are being accreted onto the main galaxies during the EoR.

Larson’s third relation describes fundamental properties of molecular clouds, relating their structures on small and large scales via two physical properties: mass and size (Larson 1981; McKee & Ostriker 2007). This is also known as the law of constant column density, since cloud mass in observations is sometimes derived by integrating over the mass surface density (Σ), which is related to the column density (N_{H_2}) obtainable from extinction maps (A_V). That is, $N_{\text{H}_2} \propto A_V$, $\Sigma \propto N_{\text{H}_2}$, and $M = \int \Sigma dA$. Therefore, cloud mass is related to N_{H_2} and A_V .

We show in Figure 12 the size-mass relation of the MCs of Althæa in the accreting phase (see §2.2) compared to the observational data of molecular clouds in the Milky Way associated with massive star formation (Beuther et al. 2002; Mueller et al. 2002; Hill et al. 2005; Motte et al. 2007) and an empirical relation obtained based on Milky Way data (Kauffmann & Pillai 2010; Kauffmann et al. 2010 and references therein), which we extrapolate to match the mass and size scales of the MCs of Althæa. By comparing the masses and sizes found in clouds with and without massive star formation ($< 10 M_\odot$)

in the Milky Way, Kauffmann et al. (2010) report a mass-size relation of $M \gtrsim 870 M_\odot \times (r/\text{pc})^{1.33}$ as the threshold for massive star formation. That is, cluster-forming cloud fragments are found to be more massive than those that are devoid of clusters at a given radius. As shown in Figure 12, the MCs identified in the accreting phase of Althæa lie above this relation, along the locus with a visual extinction of $A_V = 4$ mag. **This may suggest** On the other hand, the MCs of Althæa lie below the locus of $A_V = 100$ mag that the Milky Way clouds follow. **This may suggest** We also examine the size-mass relation of the MCs identified in other snapshots, finding that they lie in the same parameter space as the accreting phase. **so...**

Similar MC properties in relation to those observed in the nearby Universe are found for Althæa in its starburst phase (see bottom panel of Figure 5 and Figure 7).

3.3. Variation in MC Properties Depending on the Choice of Density Cuts

We investigate possible variations in the dynamics of the molecular structures of Althæa and its satellites to test the robustness of our results against the choice of density threshold by adopting different sets of n_{cut} in identifying the MCs. That is, how sensitive are the structure properties, and thus, the results presented in §3.2 dependent on the choice of density thresholds. We vary the choice of H_2 density for each of the snapshots and find no obvious differences in our results (i.e., inferences on the dynamics of $z \sim 6$ MCs in relation to those observed in nearby and $z \sim 2$ galaxies in the context of cloud scaling relations). In addition, for the densest MC in the main disk of Althæa, we find that while its size decreases as we increase n_{cut} — as one would intuitively expect, its velocity dispersion remain approximately $\sigma \simeq 200 \text{ km s}^{-1}$ (see Figure 5). This lack of variation is reassuring, in the sense that at least on the scales studied here, the dynamics of the MCs are not artifacts or biased by our choice of n_{cut} . **Our results is therefore robust, heh**

4. Origin of the clumps: Mass Scales set by Toomre and Jeans Instabilities

The onset of gravitational instability is considered to be tightly connected to (the conditions for) star formation (e.g., Kennicutt 1989; Li et al. 2005, 2006) and is widely discussed in the context of the Toomre stability criterion (Toomre 1964; Goldreich & Lynden-Bell 1965). For axisymmetric mode ($m=0$), the dispersion relation for the growth of density perturbation in a rotating turbulent disk of finite thickness h is described by:

$$\omega^2 = \kappa^2 - \frac{2\pi G \Sigma |k|}{1 + |k|h} + \sigma^2 k^2, \quad (11)$$

where k is the wavenumber in the disk and κ is the epicyclic frequency. The first term on the RHS describes rotation support, second term describes self-gravity, and the third term describes pressure support. The epicyclic frequency is defined

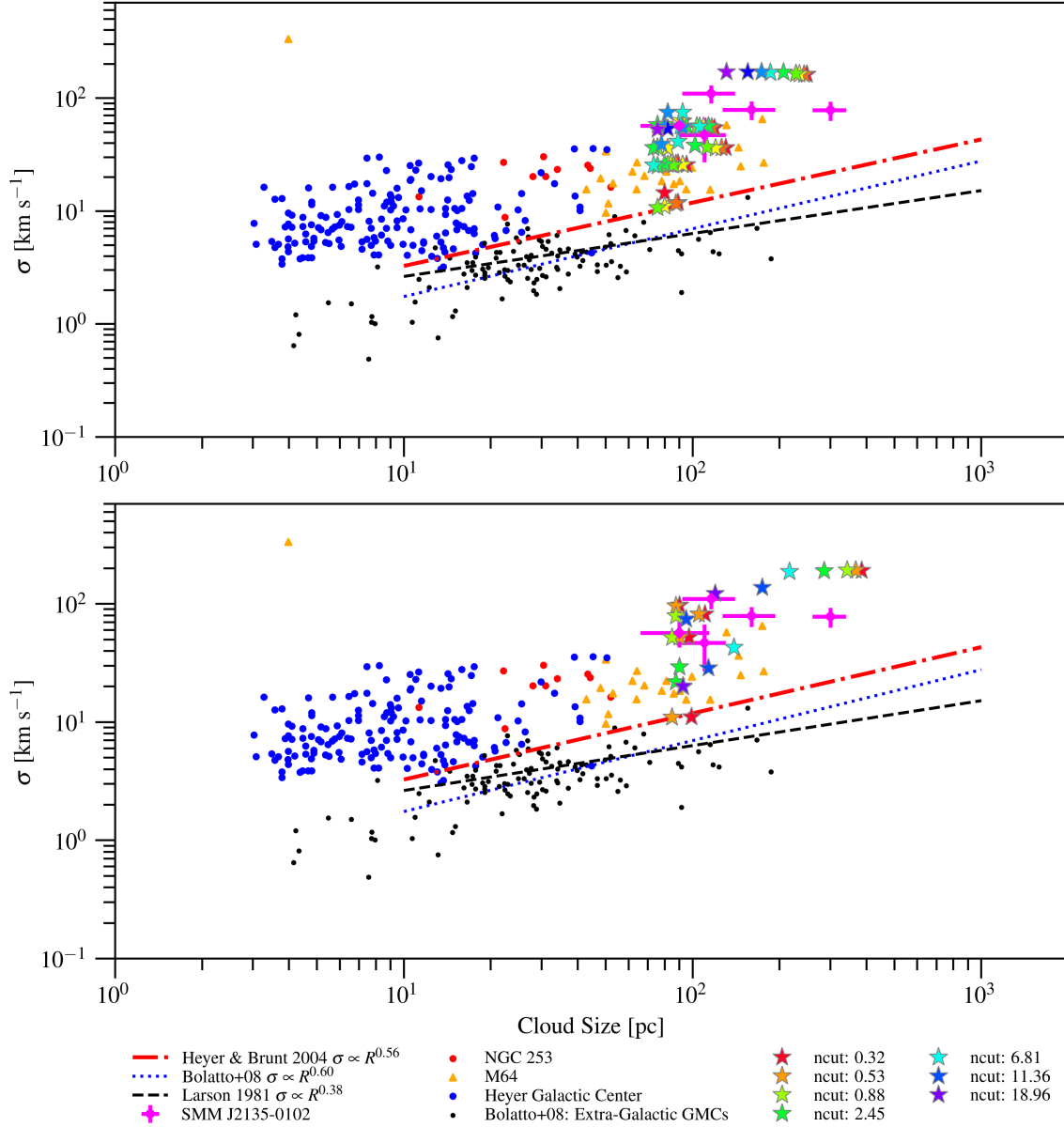


Figure 5. Larson's (linewidth-size) relation of Althaea in accreting phase (top) and starburst phase (bottom) compared to those observed in nearby and the $z \sim 2$ star-forming galaxy. Literature data and empirical relations are compiled from Larson (1981); Heyer & Brunt (2004); Rosolowsky & Blitz (2005); Bolatto et al. (2008); Swinbank et al. (2011); Leroy et al. (2015).

as:

$$\kappa^2 \equiv \frac{2\Omega}{R} \frac{d}{dR} (R^2 \Omega). \quad (12)$$

can then define the so-called Toomre-Q parameter/criterion for stability as

$$Q \equiv \frac{\sigma \kappa}{\pi G \Sigma}. \quad (13)$$

We can then rewrite Equation 11 in terms of

$$\omega^2 = Q^2 k^2 \left(\frac{\pi G \Sigma}{\kappa} \right)^2 - 2\pi G \Sigma |k| + \kappa^2. \quad (14)$$

Thus, for $Q \lesssim 1$, disk is unstable for some k ($\omega^2 < 0$) and fragmentation can happen (e.g., instability imposed by angular momentum from gas accretion from the cosmic web and satellite

galaxies and stellar feedback). That is, local fragmentation takes place when gravity overcomes pressure support from turbulence (thermal is small here) and shearing of differential rotation.

In the limit of a thin rotating disk, rotation can help stabilize self-gravitational contraction for wavelengths greater than the Toomre length:

$$\lambda_T = 4\pi^2 G \Sigma / \kappa^2, \quad (15)$$

yielding a characteristic mass of $M_T = \frac{\pi}{4} \lambda_T^2 \Sigma = 4\pi^2 \frac{G^2 \Sigma^3}{\kappa^4}$, which sets the “upper limit” to which MCs can form in a shearing disk.

yet to make the “Q”-map

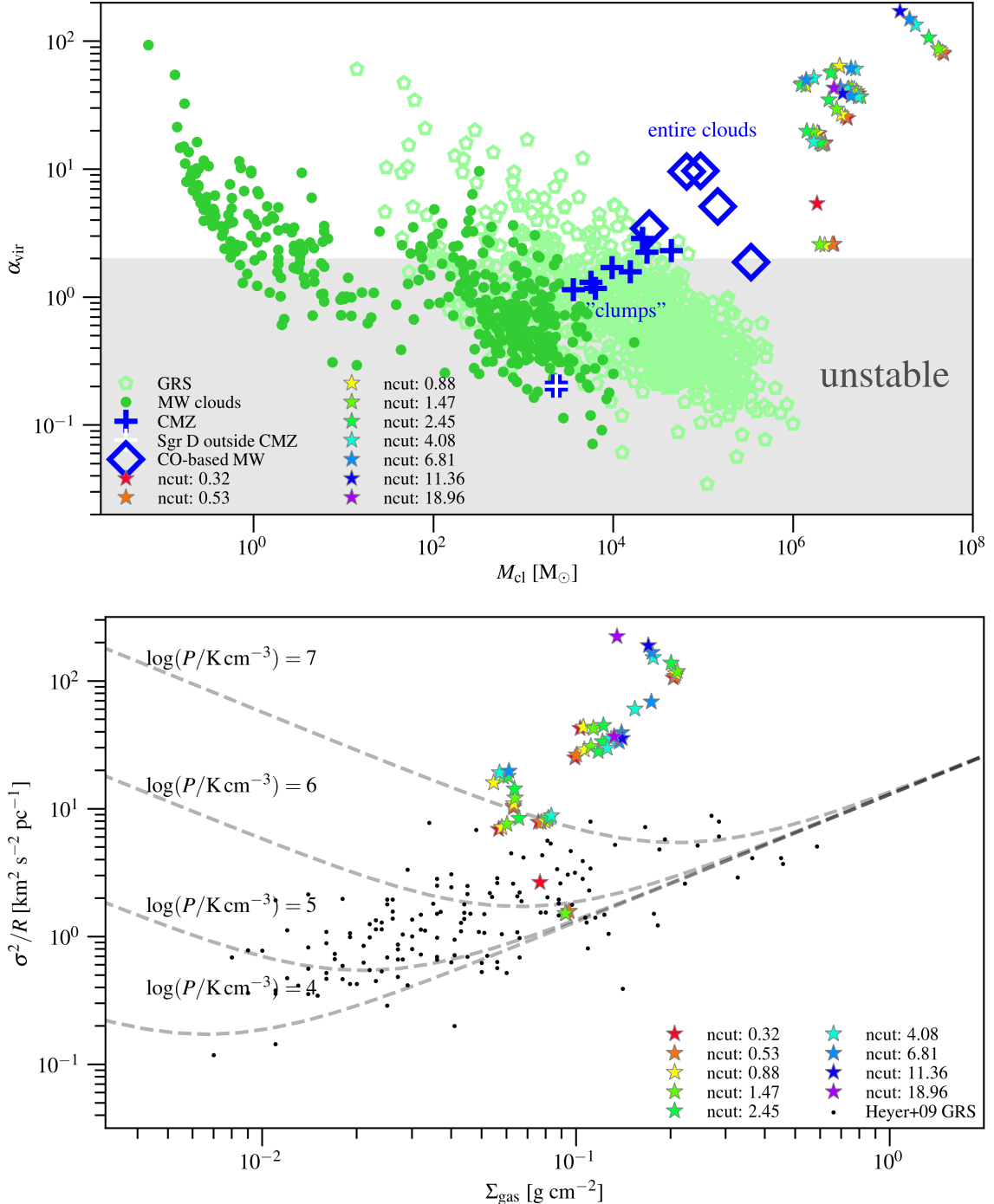


Figure 6. Top: Virial parameter and cloud mass of Althaea in the accreting phase (star symbols) compared to those observed in the Milky Way. Literature data are compiled from Kauffmann et al. 2017 and references therein. Bottom: $\sigma^2/R - \Sigma_{\text{gas}}$ relation of the MCs identified in our simulation (star symbols) compared to those observed in the Milky Way (black dot markers). The V-shaped dashed lines show the locii along which the given external pressures are needed for MCs to have linewidth σ for a given set of surface densities (see §3.1). In both panels, the star symbols are color-coded by n_{cut} . Star symbols lying close to $\alpha_{\text{vir}} \approx 2$ in the top panel and the locus of $\log(P/\text{K cm}^{-3}) = 6$ in the bottom panel correspond to MCs identified in the satellite galaxies.

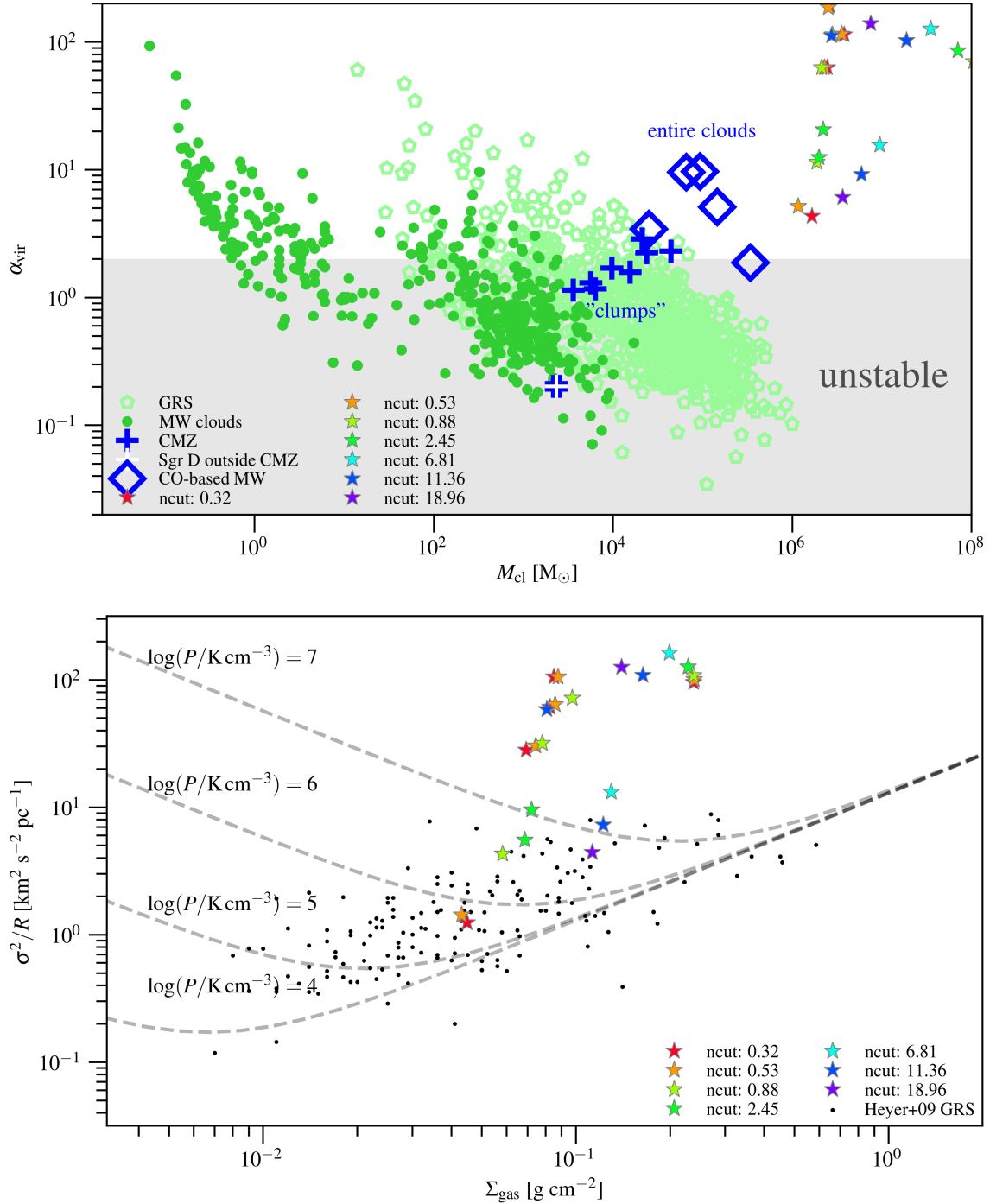


Figure 7. Same as Figure 6, but for MCs identified in the starburst phase of Althæa.

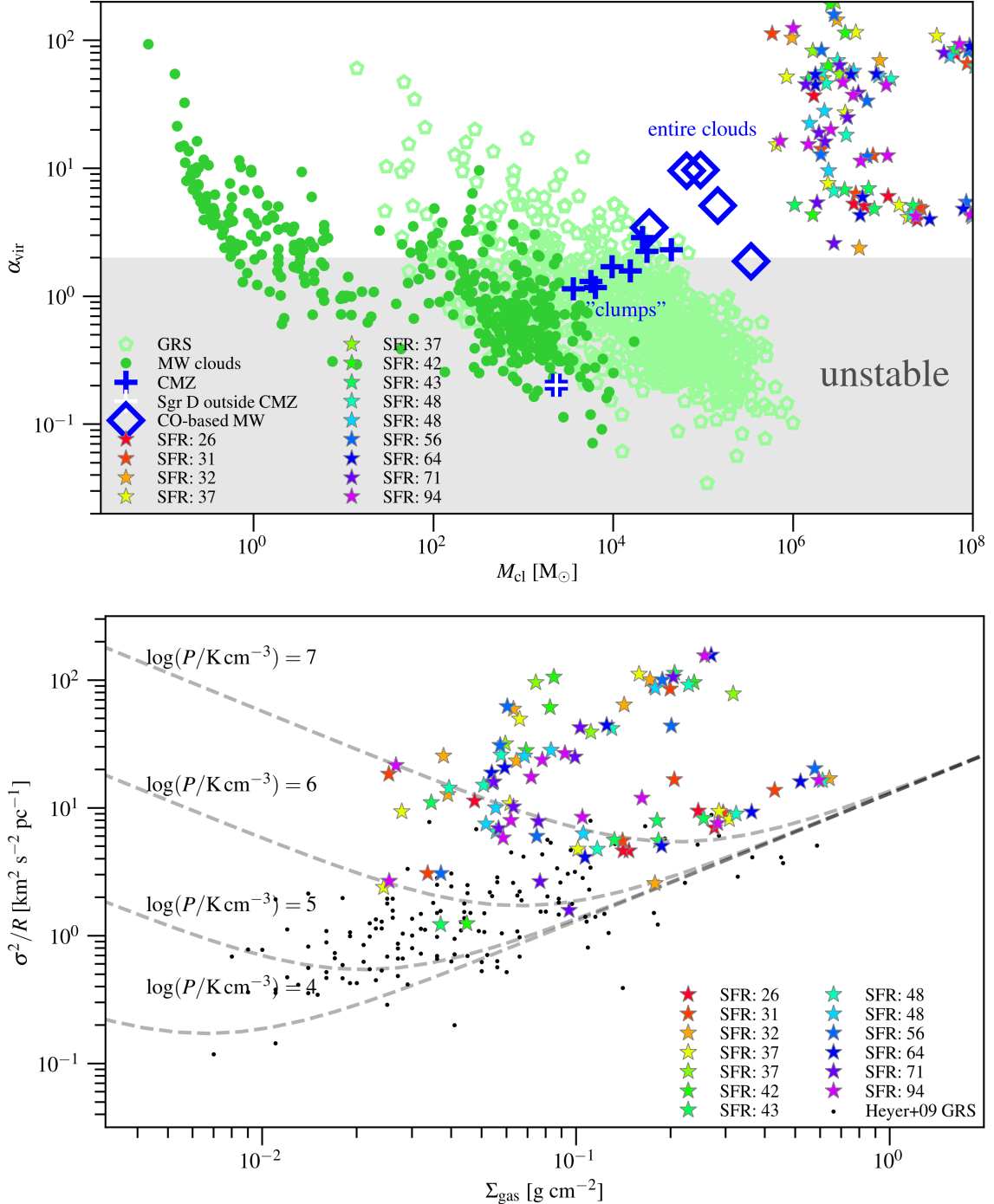


Figure 8. Same as Figure 6, but for MCs identified across all snapshots. Star symbols are color-coded by increasing SFR.

We overplot the MCs on the Toomre-Q map.

5. Cumulative Mass Distribution

The mass range of the MCs identified in our simulation is $M_{\text{cl}} \approx 10^{6.5-9} M_{\odot}$, consistent with those observed in $z \sim 2$ galaxies in rest-frame UV and optical light (Elmegreen et al. 2007, 2009). Observational studies in the nearby Universe, where spatially resolution are better at revealing molecular (sub-)structures, often report the mass distribution of molecular clouds in the form of a cumulative function (CMF). While

the CMF of the MCs for a given snapshot of our simulation is quite noisy, since we have only one (main) galaxy, we could improve the “signal-to-noise ratio” by including MCs identified across all snapshots¹⁴. We show the resulting CMF in Figure 13.

Motivated by the observational study by Blitz et al. 2007, we fit a power-law to the CMF, which is expressed in the form

¹⁴ This approach is valid unless in some snapshots, the galaxy experience a violent event, which is relatively rare across the 700 Myr studied here.

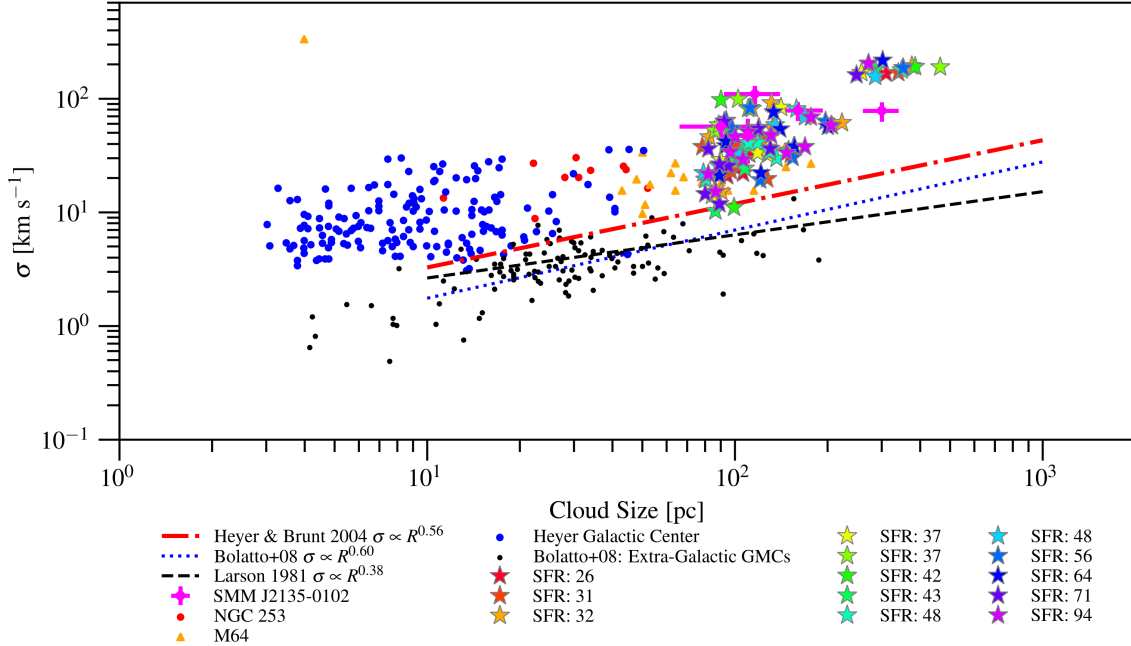


Figure 9. Comparison of the MCs of Althaea identified across all snapshots over the course of 700 Myr (star symbols) to those observed in nearby and the $z \sim 2$ star-forming galaxy in the context of the linewidth-size relation — showing variations in their properties at the different evolutionary phases of Althaea and with varying SFRs.

of:

$$n(M' > M) \propto M_{\text{cl}}^{\alpha}, \quad (16)$$

where n is the number of MCs with masses exceeding M_{cl} and α is the power-law index. The slope varies from -0.49 ± 0.01 to -1.17 ± 0.06 by adopting the lowest and the highest n_{cut} studied here. The uncertainties are the formal fitting uncertainties. Regardless of the density threshold adopted, the slope of the CMF of Althaea (Figure 13) is shallower compared to those observed in nearby galaxies (between -1.6 and -2.5 ; based on a sample of ~ 70 resolved GMCs in M31, M33, IC10 and the Magellanic Clouds; Blitz et al. 2007). This suggests that the MCs of Althaea are more massive compared to those observed in the nearby Universe.

Velocity dispersion and surface density are tightly connected to pressure. That is, the pressure of an MC is expected to increase with its velocity dispersion and surface density (see e.g., Equation 9 and since $P \propto \Sigma^2$). In the central molecular zone of the Milky Way (CMZ), we have seen molecular clouds with high pressures of $P/k_B > 10^7$ K cm $^{-3}$. Such high pressures are also seen in massive star-forming regions such as 30 Doradus. The higher Σ_{gas} in turn is related to more massive clouds being formed. In M64, there are a few clouds with masses $M_{\text{cl}} > 10^7 M_{\odot}$. On the other hand, such massive molecular structures are unknown to local group, and are likely the sites from which massive star clusters or OB associations are to be formed.

One should, however, keep in mind that the slope of the CMF reported here is subject to the uncertainties in the analysis method and the resolution of our simulation. That is, we are likely biased to finding more massive clouds due to res-

olution effects; it is possible that we may identify more and less massive MCs if our simulation was done at a higher resolution. That said, one must acknowledge that such a zoom-in simulation is currently too expensive to perform with existing computational power. In any case, similarly massive molecular clouds have been reported in simulations done at higher resolution (in closed box simulations;). It is therefore conceivable that our results are not that far off in spite of the limited resolution ($l \approx 30$ pc). Future higher resolution zoom-in simulations would certainly be useful to understand the evolving dynamical properties of the lower-mass molecular structures in galaxies at EoR under the influence of gas inflow/outflow (i.e., accounting for energy injection at large scale due to infall/outflow).

6. Discussions and Implications

6.1. Origin of the MCs

The largest molecular structure identified is essentially the main disk of Althaea, which is “broken” down into smaller spatial and mass structures that are also denser as we increase n_{cut} . In any case, the MCs we identified are much bigger in size and mass than nearby GMCs, which is consistent with those observed in $z \sim 2-4$ galaxies based on spatially resolved imaging.

The high pressure observed in Althaea is also comparable to what has been observed in local ULIRGs; however, the molecular clouds in the latter are concentrated within their central regions and have typical sizes of $\sim 70-100$ pc and masses on the order of $\sim 10^9 M_{\odot}$ (Downes & Solomon 1998; Sakamoto et al. 2008). In our simulation, the high pressure MCs of Althaea are found throughout the disk. This difference

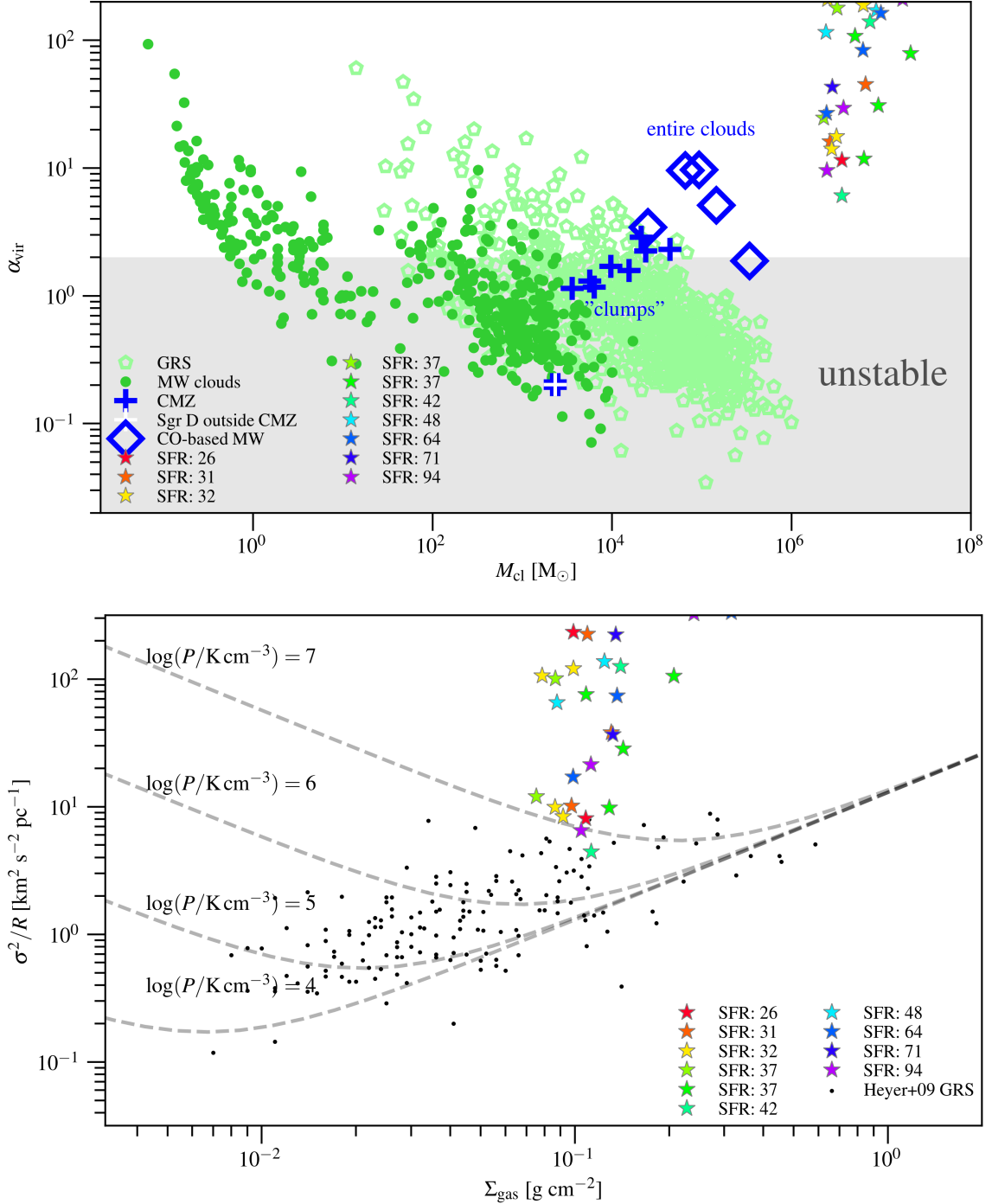


Figure 10. Same as Figure 8, but only the denser substructures of the main disk of Althaea are included (i.e., MCs here are identified with the highest n_{cut}).

likely stems from the different physical mechanisms giving rise to the formation (and thus the nature) of these molecular structures. For instance, in local ULIRGs, they are probably form by shock compression or cloud-cloud collision after the large amount of gas from the progenitor galaxy merger is being funneled toward the central region (Tan 2000; Wu et al. 2018), whereas in Althaea, which is actively accreting gaseous materials from the surrounding, they are probably form from constant cold gas accretion onto the entire galaxy (without

requiring gas to be funneled into the central region). This latter mechanism may also be the dominant mode for forming the highly supersonic massive MCs observed in gas-rich star-forming galaxies at $z \sim 2$ (see also e.g.,). The constant inter-cloud collision as gas is being accreted onto the main galaxy would also render the MCs to be gravitationally unbound (see e.g., Dobbs et al. 2011), which would be consistent with/explain the high α_{vir} found for the MCs in the main disk of Althaea.

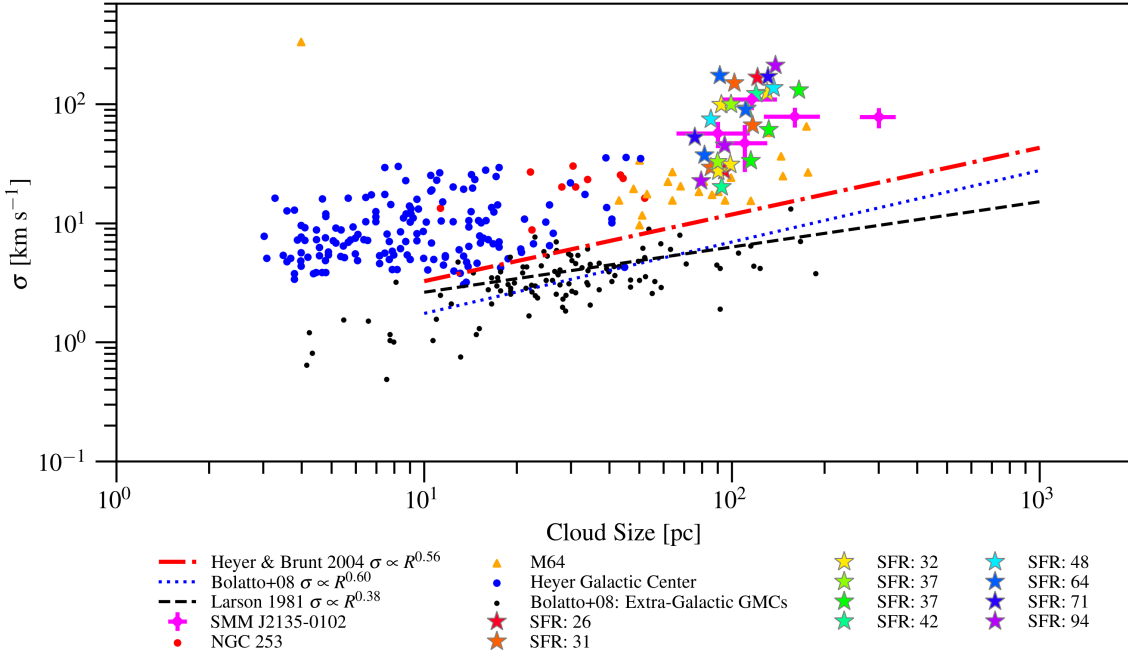


Figure 11. Same as Figure 9, but only the denser substructures of the main disk of Althaea are included (i.e., MCs here are identified with the highest n_{cut}).

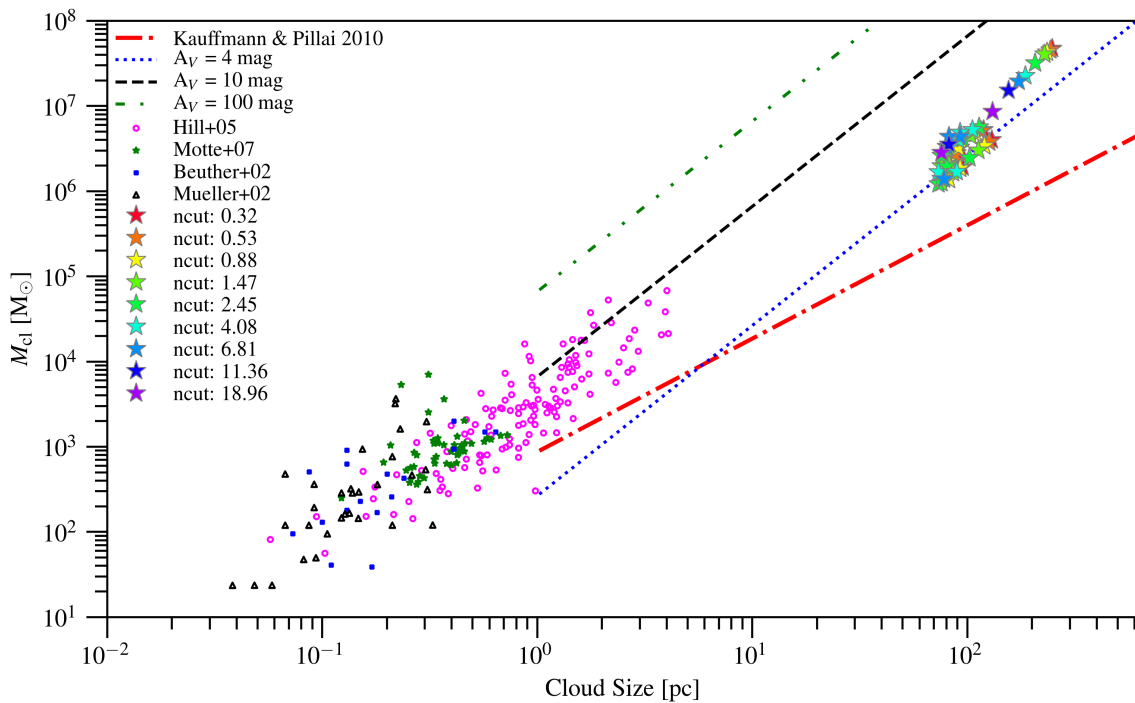


Figure 12. Size-mass relation of MCs identified in the accreting phase of Althaea in our simulation (star symbols) compared to observational data of molecular clouds in the Milky Way associated with massive star formation (magenta circles, green stars, blue dots, and black triangles) and empirical relations established based on observations of the Milky Way. Star symbols are color-coded by increasing n_{cut} . Literature data are compiled from Beuther et al. (2002); Mueller et al. (2002); Hill et al. (2005); Motte et al. (2007). Red line shows the threshold for massive star formation reported by Kauffmann & Pillai (2010).

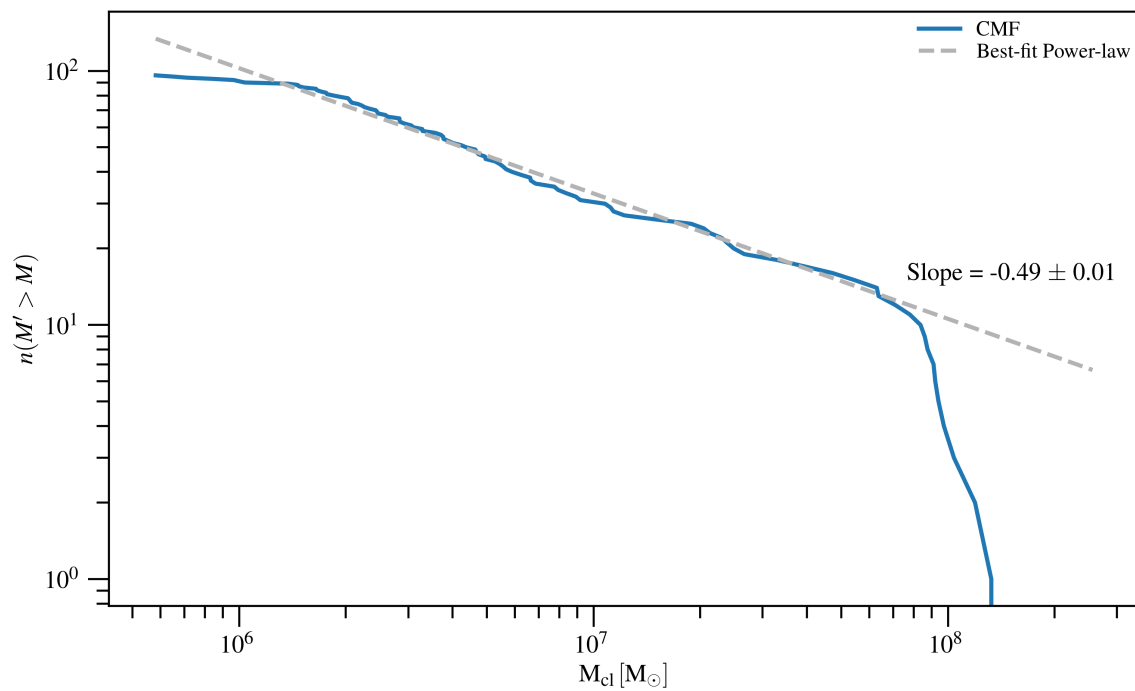


Figure 13. CMF of MCs in Althaea and best-fit power law.

6.2. Virial Parameter, Collapse, and high SFR at high- z

While it may appear that there is an inconsistency between the high α_{vir} nature of the majority of the molecular gas in Althæa and its SFR. That is, if most of the molecular gas in Althæa has high α_{vir} , why does it sustain its high SFR of $\sim 100 M_{\odot} \text{ yr}^{-1}$? This discrepancy can be explained in two ways. First, our results are limited by the resolution of the simulation, such that, in each MC, there likely exist multiple smaller-scales molecular structures (e.g., clumps and cores), as in the classical MC hierarchy. These smaller structures are no longer supported by large-scale gravitational potential and differential rotation, as turbulence has dissipated rapidly on these smaller scales to enable collapse (Clark & Bonnell 2004). In addition, non-axisymmetric perturbations (e.g., arms) to the gravitational potential can induce orbit crossing, shocks and dissipation in gas, promoting turbulence dissipation.

We note that in a recent study by Pettitt et al. (2018), the authors report that the virial parameter could be a poor indicator for the star-forming capacity of the massive ($10^{5-6} M_{\odot}$) “clouds” in their simulation. In particular, these authors do not find any significant correlation between α_{vir} and cloud mass and the star formation efficiency (M_{*}/M_{cl}). Identifying a new diagnostic tool is beyond the scope of this paper.
 Instead, we are more interested in comparing the clouds dynamics with observational studies, and thus, part of the discussion presented in this paper is based on virial analysis.

6.3. CMF and IMF at EoR

While first stars and galaxies are cooled predominated via H₂ lines. As shown in the $T - n$ phase plot in Fig. 8 of Pallottini et al. 2017a, metals also play an important role in the cooling of early galaxies.

CMF influences the IMF because .. different cooling properties will lead to different xxx, and thus, Jeans mass/thus determines the final properties of the cl[] fragmentation.... For instance, massive protostellar clumps are always supersonic, thus their internal structure are complex. They may form multiple stars.

The minimum clump mass M_{min} is limited by numerical resolution of our simulation. We do not have a resolution study (in hand) and so we cannot quantitatively evaluate this at the moment. The minimum clump mass allowed by our clump finding algorithm is the mass over 10 cells that exceeds the given threshold density.

7. Summary and Conclusions

We study the dynamical properties of molecular clouds complexes and their temporal evolution in a $z \sim 6$ prototypical galaxy at the EoR using state-of-the-art cosmological zoom-in simulation (SERRA), which includes a chemical network to determine the formation of molecular hydrogen, heating and cooling of the ISM by metals, and stellar feedback. We use a clump finder algorithm and a set of H₂ volumetric den-

sities to identify MCs and their sub-structures in the main galaxy — Althæa — of the simulated 20 Mpc h⁻¹ box and in its satellites. We decompose the molecular structures into non-overlapping tiles by identifying a set of different density contours at different snapshots. Using volumetric H₂ is essentially the same as identified molecular structures using different contours in line emission (e.g., CO, CS, NH₃) since the line luminosity scales with the molecular gas density (modulo optical depth effects). We extract properties such as mass, size, Mach number, velocity dispersion, gas surface density, and virial parameter for each MC and compare them with those observed in the Milky Way disk, the Galactic center, and gas-rich starburst galaxies in the local universe and at the peak epoch of cosmic star formation. We also examine their properties at the different evolutionary stages of Althæa and compare them with observations.

We find that the MC of Althæa are highly supersonic, with high velocity dispersions ($\sigma \approx 200 \text{ km s}^{-1}$) comparable to those observed in $z \sim 2$ starburst galaxies. The mass scale of the MCs is of the order of $10^{6.5-9} M_{\odot}$. The $\sim 200 \text{ pc}$ -scale MCs found with a low density threshold correspond to the arms of the disk of Althæa which break down into smaller $\lesssim 100 \text{ pc}$ -scale MCs at higher density thresholds. The more massive and bigger MCs in Althæa compared to the Milky Way likely result from the higher gas mass fraction, surface density, and velocity dispersion, which set the scale for fragmentation. This is consistent with what has been found previously in higher resolution simulation of isolated galaxies (). That said, our cosmological zoom-in simulation here allows us to examine the influence on the dynamics of MCs due to continuous gas accretion from the surrounding IGM (see e.g., Klessen & Hennebelle 2010; Goldbaum et al. 2011).

We compare the dynamics of MCs in Althæa to observations in the context of the Larson’s relation. The MCs of Althæa are found to have higher σ and Σ systematically regardless of the n_{cut} adopted. Our results are thus robust/insensitive to the various density cuts of choice. The velocity dispersion remains $\gtrsim 100 \text{ km s}^{-1}$ even when we increase the n_{cut} and even for the molecular substructures, likely resulting from the strong supernova and stellar feedback Althæa experienced over the multiple episodes of bursty star formation. Virial analysis indicates that the MC/arms of the main disk of Althæa are unbound, but the substructures have lower virial parameter. This is consistent with the notion that collapsing structures result from gravitational instability within globally stable structures, which are supported by turbulence and rotation on large scale. We also find $\alpha_{\text{vir}} \sim 1$ for the MCs in the satellite galaxies, which we interpret as a result of the weaker stellar feedback as they have experienced less episodes of star formation compared to Althæa (also supported by the lower stellar-to-gas mass ratio of the latter). MCs in the satellites are therefore likely collapsing structures. This paints a picture, in which at the EoR, star formation continues as gas is being accreted from the IGM. We find no temporal variations

in the MC dynamics over the course of 700 Myr traced in our simulation, at least in terms of the scaling relations examined. Our results are independent of the volume density threshold adopted, except for the slope of the cumulative mass distribution, which steepens as we increase n_{cut} .

Determining the multi-phase ISM properties of early galaxies is a critical piece to understanding the evolution and assembly history of galaxies, since they set the pace for chemical reactions and excitation rates for the coolants in the ISM (and subsequent star formation). Observations leveraging the combination of spatio-spectral imaging of multi-band continuum and spectral line emission are crucial for better understanding the role of high- z galaxy populations in the context of galaxy evolution and the ISM physics behind their intense star formation in the early universe (if only the ALMA TAC will give us to the time to do so)...

High resolution zoom-in simulations, such as SERRA, while inherently limited in galaxy statistics and is subject to the input model/sub-grid models adopted, provide an avenue to examine and postulate/make testable predictions on the morphology and dynamics of the multi-phase ISM structures of the first galaxies and their satellite galaxies. High

resolution imaging of the molecular gas content in the first galaxies with ALMA and the ngVLA, on the other hand, have the potential to provide useful observational data to test our findings and the validity of our simulation to shed light on star formation since the cosmic dark ages.

We thank Jens Kauffmann, Thushara Pillai, and Mark Swinbank for sharing their data. T.K.D.L. acknowledges support by the NSF through award SOSPA4-009 from the NRAO and support from the Simons Foundation. A.F. acknowledges support from the ERC Advanced Grant INTERSTELLAR H2020/740120. This work was initiated as a project for the Kavli Summer Program in Astrophysics (KSPA) held at the Center for Computational Astrophysics of the Flatiron Institute in 2018. The program was co-funded by the Kavli Foundation and the Simons Foundation. We thank the KSPA Scientific and Local Organizing Committees, and the program founder, Pascale Garaud for supporting the genesis of this work. We also thank the New York University CCPP for their hospitality in hosting us, the refugees, after the steam pipe explosion in NYC during the KSPA.

-
- Ballesteros-Paredes, J., Hartmann, L. W., Vázquez-Semadeni, E., Heitsch, F., & Zamora-Avilés, M. A. 2011, *MNRAS*, **411**, 65
 Ballesteros-Paredes, J., & Mac Low, M.-M. 2002, *ApJ*, **570**, 734
 Beaumont, C. N., Offner, S. S. R., Shetty, R., Glover, S. C. O., & Goodman, A. A. 2013, *ApJ*, **777**, 173
 Behroozi, P. S., Wechsler, R. H., & Conroy, C. 2013, *ApJ*, **770**, 57
 Beuther, H., Schilke, P., Menten, K. M., et al. 2002, *ApJ*, **566**, 945
 Blitz, L., Fukui, Y., Kawamura, A., et al. 2007, *Protostars and Planets V*, 81
 Bolatto, A. D., Leroy, A. K., Rosolowsky, E., Walter, F., & Blitz, L. 2008, *ApJ*, **686**, 948
 Bouché, N., Cresci, G., Davies, R., et al. 2007, *ApJ*, **671**, 303
 Bouwens, R. J., Illingworth, G. D., Labbe, I., et al. 2011, *Nature*, **469**, 504
 Bovino, S., Grassi, T., Capelo, P. R., Schleicher, D. R. G., & Banerjee, R. 2016, *A&A*, **590**, A15
 Ceverino, D., Dekel, A., & Bournaud, F. 2010, *MNRAS*, **404**, 2151
 Clark, P. C., & Bonnell, I. A. 2004, *MNRAS*, **347**, L36
 Daddi, E., Elbaz, D., Walter, F., et al. 2010a, *ApJ*, **714**, L118
 Daddi, E., Bournaud, F., Walter, F., et al. 2010b, *ApJ*, **713**, 686
 Dobbs, C. L., Burkert, A., & Pringle, J. E. 2011, *MNRAS*, **413**, 2935
 Downes, D., & Solomon, P. M. 1998, *ApJ*, **507**, 615
 Dunlop, J. S., McLure, R. J., Biggs, A. D., et al. 2017, *MNRAS*, **466**, 861
 Elmegreen, B. G., Elmegreen, D. M., Fernandez, M. X., & Lemnios, J. J. 2009, *ApJ*, **692**, 12
 Elmegreen, D. M., Elmegreen, B. G., Ravindranath, S., & Coe, D. A. 2007, *ApJ*, **658**, 763
 Federrath, C., & Klessen, R. S. 2013, *ApJ*, **763**, 51
 Ferkinhoff, C., Brisbin, D., Nikola, T., et al. 2015, *ApJ*, **806**, 260
 Gabor, J. M., & Bournaud, F. 2013, *MNRAS*, **434**, 606
 Genzel, R., Tacconi, L. J., Gracia-Carpio, J., et al. 2010, *MNRAS*, **407**, 2091
 Goldbaum, N. J., Krumholz, M. R., Matzner, C. D., & McKee, C. F. 2011, *ApJ*, **738**, 101
 Goldreich, P., & Lynden-Bell, D. 1965, *MNRAS*, **130**, 125
 Goodman, A. A., Alves, J., Beaumont, C. N., et al. 2014, *ApJ*, **797**, 53
 Grassi, T., Bovino, S., Schleicher, D. R. G., et al. 2014, *MNRAS*, **439**, 2386
 Heitsch, F., Ballesteros-Paredes, J., & Hartmann, L. 2009, *ApJ*, **704**, 1735
 Heyer, M., Krawczyk, C., Duval, J., & Jackson, J. M. 2009, *ApJ*, **699**, 1092
 Heyer, M. H., & Brunt, C. M. 2004, *ApJ*, **615**, L45
 Hill, T., Burton, M. G., Minier, V., et al. 2005, *MNRAS*, **363**, 405
 Hodge, J. A., Riechers, D., Decarli, R., et al. 2015, *ApJ*, **798**, L18
 Hodge, J. A., Swinbank, A. M., Simpson, J. M., et al. 2016, *ApJ*, **833**, 103
 Hopkins, P. F., Kocevski, D. D., & Bundy, K. 2014, *MNRAS*, **445**, 823
 Hughes, A., Wong, T., Ott, J., et al. 2010, *MNRAS*, **406**, 2065
 Hughes, A., Meidt, S. E., Colombo, D., et al. 2013, *ApJ*, **779**, 46
 Ibáñez-Mejía, J. C., Mac Low, M.-M., Klessen, R. S., & Baczyński, C. 2016, *ApJ*, **824**, 41
 Inoue, S., Dekel, A., Mandelker, N., et al. 2016, *MNRAS*, **456**, 2052
 Kauffmann, J., & Pillai, T. 2010, *ApJ*, **723**, L7
 Kauffmann, J., Pillai, T., Shetty, R., Myers, P. C., & Goodman, A. A. 2010, *ApJ*, **716**, 433
 Kauffmann, J., Pillai, T., Zhang, Q., et al. 2017, *A&A*, **603**, A90
 Kennicutt, Jr., R. C. 1989, *ApJ*, **344**, 685
 —. 1998, *ARA&A*, **36**, 189
 Klessen, R. S., & Hennebelle, P. 2010, *A&A*, **520**, A17
 Krumholz, M. R., McKee, C. F., & Tumlinson, J. 2009, *ApJ*, **693**, 216
 Larson, R. B. 1981, *MNRAS*, **194**, 809
 Leroy, A. K., Bolatto, A. D., Ostriker, E. C., et al. 2015, *ApJ*, **801**, 25
 Li, Y., Mac Low, M.-M., & Klessen, R. S. 2005, *ApJ*, **626**, 823
 —. 2006, *ApJ*, **639**, 879
 Maiolino, R., Carniani, S., Fontana, A., et al. 2015, *MNRAS*, **452**, 54
 Malhotra, S., Kaufman, M. J., Hollenbach, D., et al. 2001, *ApJ*, **561**, 766

- McKee, C. F., & Ostriker, E. C. 2007, *ARA&A*, **45**, 565
- Meidt, S. E., Schinnerer, E., García-Burillo, S., et al. 2013, *ApJ*, **779**, 45
- Motte, F., Bontemps, S., Schilke, P., et al. 2007, *A&A*, **476**, 1243
- Mueller, K. E., Shirley, Y. L., Evans, II, N. J., & Jacobson, H. R. 2002, *ApJS*, **143**, 469
- Oka, T., Hasegawa, T., Sato, F., et al. 2001, *ApJ*, **562**, 348
- Ono, Y., Ouchi, M., Curtis-Lake, E., et al. 2013, *ApJ*, **777**, 155
- Pallottini, A., Ferrara, A., Bovino, S., et al. 2017a, *MNRAS*, **471**, 4128
- Pallottini, A., Ferrara, A., Gallerani, S., et al. 2017b, *MNRAS*, **465**, 2540
- Pan, H.-A., Fujimoto, Y., Tasker, E. J., et al. 2015, *MNRAS*, **453**, 3082
- Pettitt, A. R., Egusa, F., Dobbs, C. L., et al. 2018, *MNRAS*, **480**, 3356
- Planck Collaboration, Ade, P. A. R., Aghanim, N., et al. 2014, *A&A*, **571**, A16
- Rosolowsky, E., & Blitz, L. 2005, *ApJ*, **623**, 826
- Rosolowsky, E., & Leroy, A. 2006, *PASP*, **118**, 590
- Rubin, R. H. 1985, *ApJS*, **57**, 349
- Sakamoto, K., Wang, J., Wiedner, M. C., et al. 2008, *ApJ*, **684**, 957
- Sanders, D. B., Scoville, N. Z., & Solomon, P. M. 1985, *ApJ*, **289**, 373
- Scoville, N. Z., & Solomon, P. M. 1974, *ApJ*, **187**, L67
- Shetty, R., Collins, D. C., Kauffmann, J., et al. 2010, *ApJ*, **712**, 1049
- Smit, R., Bouwens, R. J., Carniani, S., et al. 2018, *Nature*, **553**, 178
- Smith, B. D., Turk, M. J., Sigurdsson, S., O’Shea, B. W., & Norman, M. L. 2009, *ApJ*, **691**, 441
- Sparre, M., Hayward, C. C., Springel, V., et al. 2015, *MNRAS*, **447**, 3548
- Swinbank, A. M., Papadopoulos, P. P., Cox, P., et al. 2011, *ApJ*, **742**, 11
- Tacconi, L. J., Genzel, R., Neri, R., et al. 2010, *Nature*, **463**, 781
- Tan, J. C. 2000, *ApJ*, **536**, 173
- Teyssier, R. 2002, *A&A*, **385**, 337
- Toomre, A. 1964, *ApJ*, **139**, 1217
- Turk, M. J., Smith, B. D., Oishi, J. S., et al. 2011, *ApJS*, **192**, 9
- Williams, J. P., de Geus, E. J., & Blitz, L. 1994, *ApJ*, **428**, 693
- Wu, B., Tan, J. C., Nakamura, F., Christie, D., & Li, Q. 2018, *PASJ*, **70**, S57

Appendix

Schmidt-Kennicutt Relation

As benchmarking, we check the SK relation for the MCs identified based on their SFR and gas surface densities. We show in Figure 14 the MCs of Althæa, identified using different n_{cut} in the “accreting snapshot” (see §2.2 for details) compared to those reported in observations.

(AP: i'm currently a bit confused on how to re-generate pickle files to be used for the plot) (DL: by running `test_brute.py`)

(AP: I would put a figure with the SK-relation for the clumps in a single snapshot for different cuts, along with the observed points and the global Althæa point from the data found in Pallottini et al. (2017b)) (DL: to do... after getting points from Pallo, then update `plot_cloud_prop.py` and `plotsingleSS.py` (uncomment `plot_suff(SK)` and only plot snapshot 16))

Figure 14. SFR and gas surface densities of MCs identified in Althæa in SERRA (star symbols) compared to those observed in $0 \lesssim z \lesssim 2$ galaxies. Literature data are compiled from Kennicutt 1998; Bouché et al. 2007; Daddi et al. 2010b,a; Genzel et al. 2010; Tacconi et al. 2010 and Pallottini et al. 2017a.